ACS NANO
Cite This: ACS Nano XXXX, XXX, XXX–XXX
www.acsnano.org
ARTICLE

Ferritin Nanocarrier Traverses the Blood Brain Barrier and Kills Glioma

Kelong Fan,[*,†,#] Xiaohua Jia,[‡,#] Meng Zhou,[†,§,#] Kun Wang,[‡] João Conde,[∥] Jiuyang He,[†] Jie Tian,[*,‡] and Xiyun Yan[*,†,§]

[†]Key Laboratory of Protein and Peptide Pharmaceuticals, CAS-University of Tokyo Joint Laboratory of Structural Virology and Immunology, Institute of Biophysics, Chinese Academy of Sciences, Beijing 100101, China

[‡]Key Laboratory of Molecular Imaging of Chinese Academy of Sciences, Institute of Automation, Chinese Academy of Sciences, Beijing 100190, China

[§]University of Chinese Academy of Sciences, 19A Yuquan Road, Beijing 100049, China

[∥]School of Engineering and Materials Science, Queen Mary University of London, London E1 4NS, U.K.

S *Supporting Information*

ABSTRACT: **Over the last decades, considerable efforts have been put into developing active nanocarrier systems that cross the blood brain barrier (BBB) to treat brain-related diseases such as glioma tumors. However, to date none have been approved for clinical usage. Here, we show that a human H-ferritin (HFn) nanocarrier both successfully crosses the BBB and kills glioma tumor cells. Its principle point of entry is the HFn receptor (transferrin receptor 1), which is overexpressed in both BBB endothelial cells (ECs) and glioma cells. Importantly, we found that HFn enters and exits the BBB *via* the endosome compartment. In contrast, upon specifically targeting and entering glioma cells, nearly all of the HFn accumulated in the lysosomal compartment, resulting in the killing of glioma tumor cells, with no HFn accumulation in the surrounding healthy brain tissue. Thus, HFn is an ideal nanocarrier for glioma therapy and possesses the potential to serve as a therapeutic approach against a broad range of central nervous system diseases.**

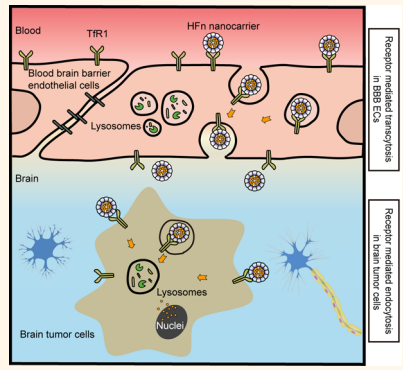

KEYWORDS: *human H-ferritin nanocarrier, blood brain barrier, transferrin receptor 1, receptor-mediated transcytosis, glioma-targeted therapy*

The blood brain barrier (BBB) represents a protective interface between the central nervous system (CNS) and peripheral blood circulation. It is mainly composed of vascular endothelial cells of the brain capillaries surrounded by pericytes and astrocytes.[1] The BBB is essential for maintaining homeostasis of the CNS and prevents entry of potential neurotoxins into the brain. Due to its highly selective permeability, the BBB also presents a formidable obstacle to the successful delivery of drugs into the brain. Both large molecules and the majority of antitumor drugs fail to pass the BBB, thus preventing effective treatment of brain-related diseases. Although dozens of new targeting biomarkers have been discovered and significantly benefit patients with peripheral tumors, none of these therapies improve the overall survival rate in brain tumor patients,[2] partly due to the fact that the presence of the BBB prevents both early diagnosis and effective drug delivery.[3] Therefore, one of the biggest challenges for successful diagnosis and therapy for brain tumors is to traverse the BBB.[4]

One promising strategy for transporting drugs across the BBB barrier is to target endogenous receptor-mediated transport (RMT) systems. One such system of highly expressed receptors in BBB endothelial cells (BBB ECs) includes three major receptors, namely, transferrin receptor 1 (TfR1), insulin receptor, and low-density lipoprotein receptors.[5]

Among these, TfR1 has been studied in great detail and thus represents a potential candidate for translational research.[6,7] Importantly, TfR1 is expressed at high levels at the BBB as well as on brain tumor tissues, and the expression levels of TfR1 on tumors correlates well with the pathological grades of brain tumors.[8,9] TfR1 mediates iron delivery to the brain *via* binding and intracellular trafficking of the iron-binding protein transferrin (Tf).[10] Due to the high concentrations of endogenous Tf present in the bloodstream, neither Tf nor Tf mimetic peptides are ideal RMT-targeting ligands, as the injected RMT delivery system would compete with endogenous Tf for TfR1 binding.[11,12] To overcome this challenge, antibodies binding to epitopes on the extracellular domain of TfR1 distal to the Tf-binding site[5] have previously been

Received: October 1, 2017
Accepted: April 2, 2018
Published: April 2, 2018

DOI: 10.1021/acsnano.7b06969
ACS Nano XXXX, XXX, XXX–XXX

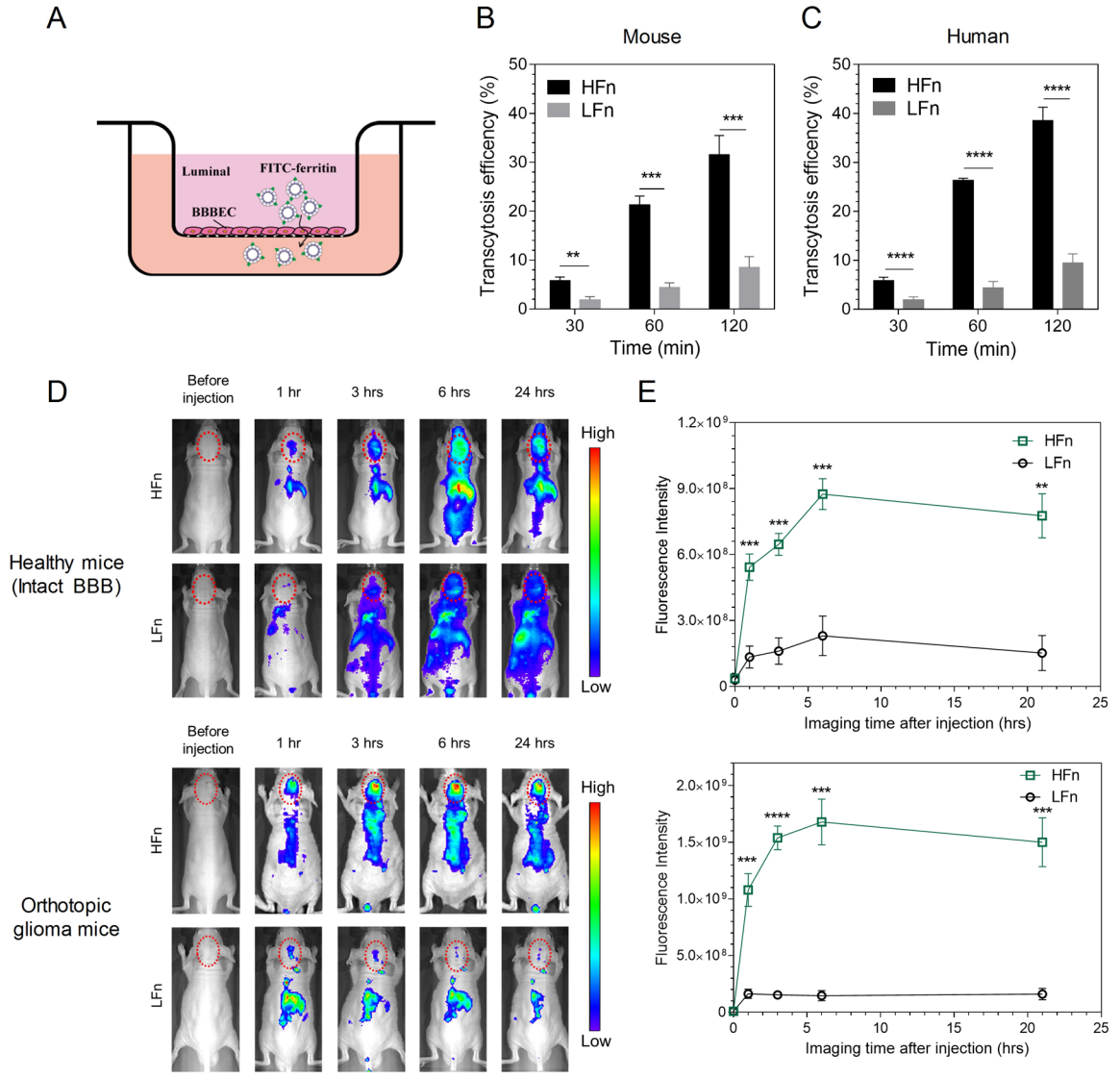

Figure 1. HFn successfully crosses the BBB and accumulates in glioma tumors. (A) Illustration of the *in vitro* BBB model. (B, C) Transcytosis of HFn and LFn in an *in vitro* BBB model: (B) mouse; (C) human. *$p < 0.05$, **$p < 0.01$, ***$p < 0.001$, ****$p < 0.0001$, unpaired Student's *t*-test. (D) *In vivo* imaging of IRdye800-HFn and IRdye800-LFn that were intravenously injected into healthy mice ($n = 3$, upper panel) and U87MG orthotopic tumor bearing mice (lower panel). Red circles indicate the brain area. (E) Quantitative analysis of the fluorescence signals of IRdye800-HFn and IRdye800-LFn in the brain area of healthy mice and glioma tumor mice. Mean ± SEM, $n = 3$. **$p < 0.01$, ***$p < 0.001$, ****$p < 0.0001$, unpaired Student's *t*-test.

developed. Despite substantial anti-TfR1 antibody binding and endocytosis into BBB endothelial cells, limited transcytosis into the brain parenchyma has been observed, primarily because of the accumulation and degradation of anti-TfR1 antibodies in the endothelial lysosomes.[7,13,14]

While tuning the binding affinities of anti-TfR1 antibodies improved intracellular trafficking and transcytosis of BBB,[13,15] such manipulation also presents several additional challenges. Fusion proteins usually possess poor stability and immunogenicity;[16] in addition, the delivery efficiency of the antibody is low and the amounts of antibodies taken up by the brain are limited.[5] An equally important point to consider is the high cost of antibody engineering, rendering this approach unfeasible for clinical use.

The development of nanotechnologies allows for new approaches for delivering therapeutics to specific target sites.[17] Combining with specific ligands, the nanocarriers are considered as one of the most promising and versatile drug delivery systems for otherwise inaccessible regions such as the brain.[18,19] Because of their ideal size, high cargo loading, controlled drug release, and suitable pharmacokinetics, nanocarriers are now considered to be powerful tools for brain disease therapy.[16,18,19] Previous reports have shown that brain-targeted nanocarrier enhanced the distribution of drugs in the brain; however, the poor selection between normal brain and diseased brain restricted the application of this strategy.[16] Dual targeting strategies using systems anchored to BBB-targeting ligands and targeted tumor cell-binding ligands are favorable to improve selective brain distribution.

Numerous efforts have been made to develop active targeting nanocarriers that cross the BBB and target glioma tumors in the last decades, and few of them reached the clinical trial stage, but none have been approved for clinical use.[1,16,18,20] Chemically prepared nanocarriers are hard to translate from bench to

DOI: 10.1021/acsnano.7b06969
ACS Nano XXXX, XXX, XXX−XXX

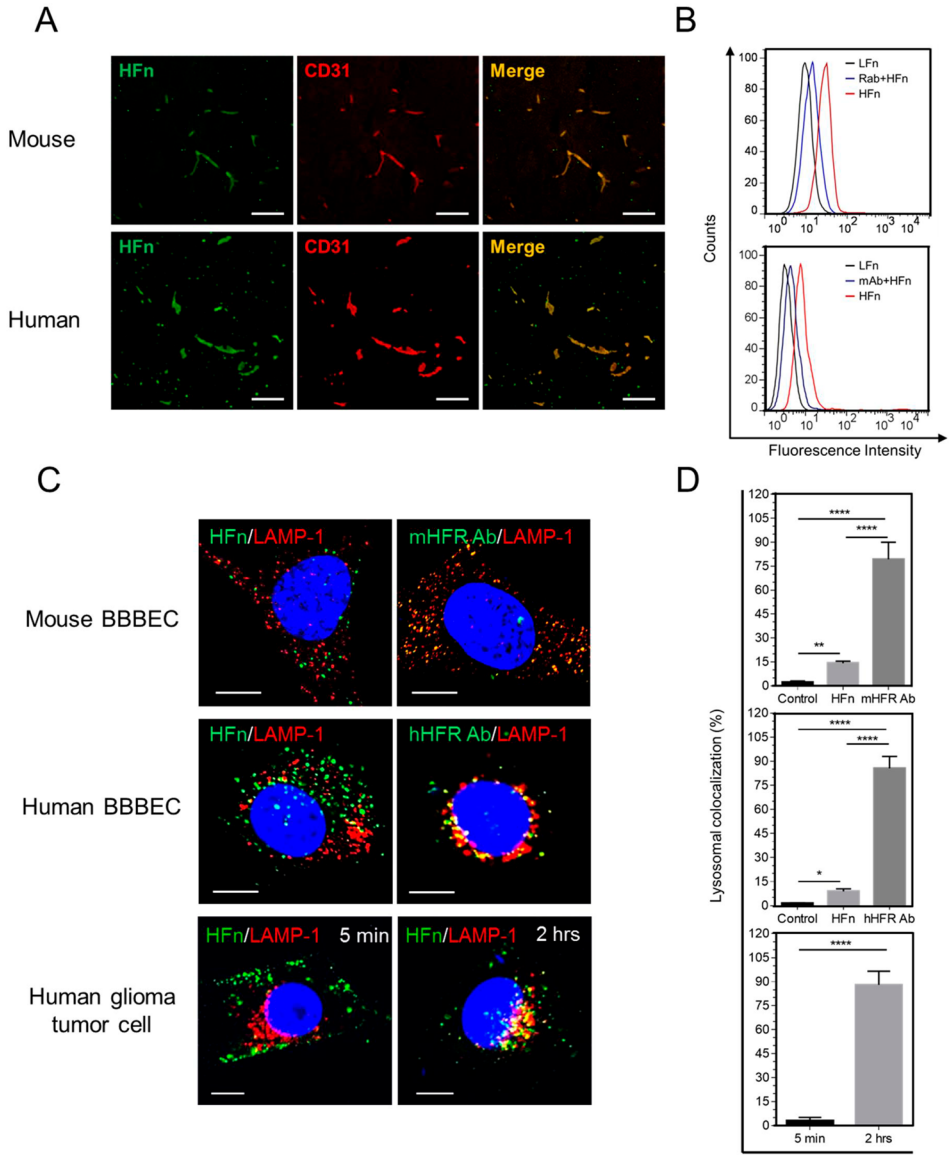

Figure 2. Specific receptor-mediated binding of HFn to BBB and subcellular localization of HFn in BBB ECs and tumor cells. (A) Immunofluorescence (IF) analysis showed that m(h)HFR (green) colocalizes with blood vessel endothelial marker CD31 (red) in normal mouse brain tissue sections (clinical human nonglioma brain tissue sections, lower panel). mHFR and hHFR were stained by FITC-labeled HFn. The Pearson colocalization coefficient of HFn and CD31 in mouse brain tissue was determined as 0.9073, and that in human brain tissue as 0.8842. Scale bar = 50 μm. (B) Antibody blocking assay to test binding of HFn to mouse BBB EC bEnd.3 cells (upper panel) and human BBB EC hCMEC/D3cells (lower panel). Rab, rabbit anti-mHFR antibody; mAb, mouse anti-hHFR antibody. (C) In normal mouse and human BBB ECs, the localization of HFn (in green: labeled with FITC, left top and middle panels; stained by anti-HFR antibody, right top and middle panels) was different from that of HFn in human glioma tumor cells (lower panel). Mouse BBB EC, bEnd.3 cells; human BBB EC, hCMEC/D3cells. Lysosomes were stained in red using the LAMP1 marker. The nuclei of cells were DAPI-stained (blue). For mouse and human BBB ECs, the subcellular localization of HFn at 4 h postincubation is shown. For glioma tumor cells, the subcellular localization of HFn at 5 min and 2 h postincubation is shown. Scale bar = 10 μm. (D) Percentage of lysosomal colocalization in BBB ECs and glioma tumor cells. For mouse and human BBB ECs, percentage of lysosomal colocalization after 4 h uptake is shown. Control, background signal was checked in the absence of protein. *$p < 0.05$, **$p < 0.01$, ****$p < 0.0001$ (one-way ANOVA with Tukey's multiple comparisons test). For human glioma cells, the percentage of lysosomal colocalization 2 h postincubation is shown. ****$p < 0.0001$, unpaired Student's *t*-test.

bedside because of their complicated synthesis procedures and long-term toxic effects. Bionanoparticles composed of natural polymers, such as amino acids or albumin, are better suited for developing biocompatible nanocarriers; however, they have other disadvantages such as batch-to-batch variability as well as limited ability for controlled modifications,[18] rendering their use challenging.

Ferritin is a natural spherical iron storage protein composed of a self-assembled 24-subunit protein shell with an outer diameter of 12 nm and interior cavity diameter of 8 nm.[21] Mammalians have two types of ferritin, namely, heavy chain ferritin (H-ferritin) and light chain ferritin (L-ferritin). Recent studies found that human H-ferritin (HFn) specifically binds to TfR1 (human HFn receptor, hHFR), and we demonstrated that HFn and Tf share the same receptor, TfR1, although they bind to different epitopes on TfR1.[22,23] Recently, we reported that HFn nanocarriers selectively deliver both loaded drugs and encapsulated iron oxide nanoparticles into peripheral tumors *in*

DOI: 10.1021/acsnano.7b06969
ACS Nano XXXX, XXX, XXX−XXX

vivo by TfR1-mediated specific targeting without additional modification of extra targeting ligands.[22,24,25] In contrast, human L-ferritin (LFn), possessing a structure similar to HFn, is unable to target malignant cells.[23,26−28]

Here, we set out to explore the capabilities of HFn transporting across the intact BBB in healthy mice and targeting glioma tumors in an intracranial orthotopic glioblastoma mouse model.

RESULTS AND DISCUSSION

HFn Traverses the BBB and Targets Glioma Tumor Cells. To investigate whether HFn possesses the ability to traverse the BBB, we performed a BBB transcytosis assay both *in vitro* and *in vivo*. In a BBB transcytosis assay using *in vitro* models constructed of either human or mouse BBB ECs (Figure 1A), we found that HFn effectively traversed both the mouse and human BBB (Figure 1B,C). In comparison, control human L-ferritin failed to traverse the BBB. The rate of HFn transport across the BBB was between 5 to 6 times higher than that of LFn after 1 h of incubation with ferritin proteins (Figure 1B,C). To evaluate whether our HFn nanocarriers are able to transcytose, we also employed a coculture model consisting of mouse BBB ECs and pericytes. The rate of HFn transport across the coculture BBB model was similar to the rate observed in the monoculture BBB model (Figure S1A,B). Importantly, we found that HFn nanocarriers maintain their intact structure after traversing the BBB (Figure S1C,D). Together, these results clearly demonstrated that HFn has the ability to traverse the BBB *in vitro*.

To test whether HFn traverses the BBB *in vivo*, we systemically administered HFn into healthy mice. As shown in Figure 1D, intravenously (i.v.) injected HFn penetrated the brain after being transported across the intact BBB. While fluorescent IRdye800-conjugated HFn was detected specifically in the brain, no significant accumulation of fluorescence signal was detected in the brain of mice administered with the same dose of IRdye800-LFn. Quantitative analysis showed that the intensity of HFn saw a 5-fold increase compared with the LFn in the brain area of mice as early as 1 h after administration (Figure 1E, healthy mouse). Moreover, the *in vivo* brain signal of IRdye800-HFn slowly increased and reached its maximum intensity at 4−6 h postinjection and persisted thereafter (Figure 1D and E), which is consistent with the elimination half-life of HFn in the blood of healthy mice.[24,25] Histopathologic analysis (see Figure S2) showed that, after penetrating the BBB, HFn accumulated in the brain parenchyma area, as measured by Prussian blue staining of magneto-HFn in this location. In comparison, we did not detect any chromogen signal in the brain sections of mice administrated with magneto-LFn, indicating that control LFn was unable to penetrate the BBB *in vivo*. Taken together, our results indicated that i.v.-injected HFn successfully traverses the BBB.

In order to explore whether HFn targets glioma tumor cells after traversing the BBB *in vivo*, we employed an orthotopic mouse model bearing luciferase-expressing human glioma tumor U87MG to perform the analysis.

As shown in Figure 1D (tumor bearing mice), i.v.-injected HFn nanocarriers quickly accumulated in the brain area, with kinetics similar to that observed in healthy mice. Intriguingly, the accumulated HFn did not distribute evenly throughout the brain; instead, it localized specifically within the bioluminescent U87MG tumor (Figure S3A). No significant accumulation of fluorescence signal in the brain area was detected in the control experiment (Figure 1D).

Quantitative analysis of the fluorescent signal showed that the HFn accumulation in the brain of glioma-bearing mice was more than 10-fold higher than that of LFn in control mice across all four time points ($p < 0.0001$ at 3 h postinjection and $p < 0.001$ at other time points postinjection, Figure 1E). Similar to the kinetics of HFn accumulation in normal mice, HFn enrichment in the brain area of glioma U87MG-bearing mice reached its maximum at 4−6 h postinjection and was maintained thereafter (Figure 1E). These observations indicated that, following BBB crossing, HFn specifically targets glioma tumor cells.

Transcytosis of HFn Mediated by Its Receptor. As most biologics cannot be passively delivered across the BBB, receptor-mediated transcytosis constitutes a promising alternative, e.g., TfR1-mediated transport of Tf across the BBB.[5] We have previously shown that HFn can act as an endogenous ligand of TfR1 and be targeted to non-brain tumor cells[22] for tumor diagnosis[22] and therapy;[24] thus we proposed that HFn overcomes the BBB *via* receptor-mediated transport.

To confirm our hypothesis, we first tested whether BBB ECs express HFRs by performing immunofluorescence staining experiments. As shown in Figure 2A, the staining of FITC-labeled HFn with healthy mice brain sections and human clinical nontumor brain tissue sections were colocalized with brain endothelial cells, indicating that brain ECs express HFR (HFn receptor). The expression of mHFR in BBB ECs was confirmed by colocalization analysis (Figure S4D). In addition, both mouse HFR (mHFR, TIM-2) and human HFR (hHFR, TfR1) were shown to be highly expressed in the ECs of BBB (Figure S4), and anti-m(h)HFR antibodies significantly decreased the binding of HFn to mouse (human) BBB ECs. Together, these results indicate that HFR is highly expressed in BBB ECs (Figure 2B).

Previous studies indicated that, following uptake by either HFR-positive T cells or kidney cells, HFn transits through the endosome and eventually enters the lysosomal compartment.[23,29,30]

In order to determine the intracellular location of HFn in EC cells of the BBB, we performed an immunofluorescence assay. We first exposed mouse bEnd.3 cells to HFn, LFn, and anti-mHFR antibody, respectively, at equal concentrations for 2 h to allow mHFR binding, internalization, and intracellular sorting, before identifying the location of these proteins. HFn started to localize specifically on the cell membrane of bEnd.3 shortly after incubation (Figure S5C, left). After a 2 h incubation, the majority of the internalized HFn nanocarriers were located in the vesicles in the cytoplasm of mouse BBB ECs (Figure 2C, upper left panel). No significant binding of LFn to bEnd.3 was observed in the control experiment (Figure S5C, right). Less than 15% of the internalized HFn colocalized with lysosome-associated membrane protein (Lamp-1) (Figure 2D, upper panel), indicating that very little HFn reached the lysosome compartment. In contrast, the high level of colocalization (more than 76%) of anti-mHFR antibody and lysosomes indicated that the antibodies were primarily sorted to the lysosome compartment after cell entry (Figure 2C, upper right panel; Figure 2D, upper panel). Subcellular localization of the internalized HFn in human BBB ECs (hCMEC/D3) was similar to that observed in mouse BBB ECs. Most internalized HFn nanocarriers were found to be located in the cytoplasm, with little signal detected in the lysosomes (Figure 2C, middle

DOI: 10.1021/acsnano.7b06969
ACS Nano XXXX, XXX, XXX−XXX

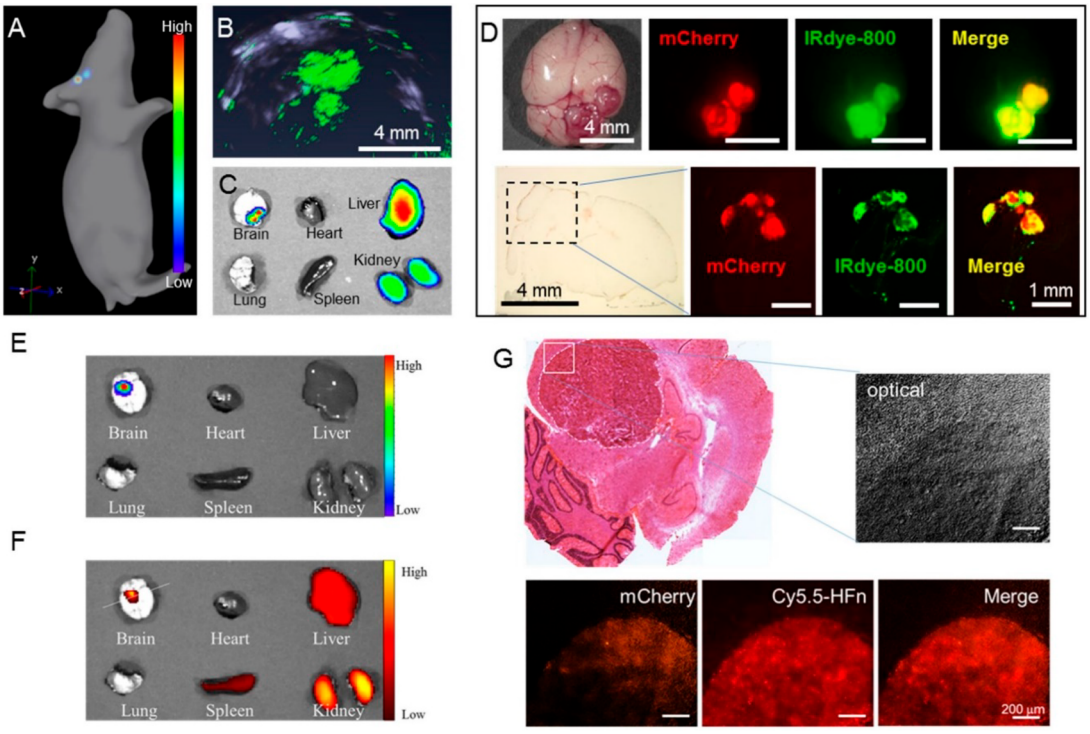

Figure 3. Injection of HFn results in its accumulation in glioma tumors, whereas normal brain tissues remain HFn-free. (A) 3D bioluminescence tomography of orthotopic glioma tumors based on the BLI signal of U87MG *in vivo*. (B) Photoacoustic imaging of U87MG-bearing mouse *in vivo* after i.v. injection of IRdye800-HFn. Scale bar = 4 mm. (C) *Ex vivo* NIRF imaging of the main organs of U87MG orthotopic mice. (D) Brain (upper panel, scale bar = 4 mm) and brain section (lower panel, scale bar = 1 mm) in the whole *ex vivo* tumor bearing mouse. The dashed rectangular area of the brain section was zoomed in for details. (E) *Ex vivo* bioluminescence imaging of the main organs of U87MG orthotopic tumor bearing mouse. (F) *Ex vivo* NIRF imaging of the main organs of orthotopic tumor bearing mouse after intravenous injection of Cy5.5-HFn nanoparticles. (G) Confocal imaging and HE staining analysis of the sections U87MG orthotopic tumor after administration of Cy5.5-HFn. Scale bar = 200 μm.

left panel; Figure 2D, middle panel). In contrast, anti-HFR antibodies were mainly sorted to the lysosomal compartment, which is consistent with previous studies (Figure 2C, middle right panel; Figure 2D, middle panel).[13,14] The intracellular distribution of HFn nanocarriers in endothelial cells of both mouse and human BBB (Figure 2C, D) suggests that HFn crosses the BBB *via* HFR-mediated RMT. Together, these results support the assumption that HFn acts as a ligand of HFR and crosses the BBB *via* HFR-mediated RMT (Figure S6).

Since HFn specifically accumulated in the brain tumor sites, we investigated the subsequent subcellular localization of HFn in U87MG tumor cells. Expression levels of hHFR were confirmed for human glioma cell U87MG by flow cytometry analysis (Figure S5A). The specific binding of HFn and U87MG cells was analyzed by flow cytometry and immunofluorescence (IF) (Figure S5B and D). Surprisingly, more than 90% of all lysosomes contained HFn after a 2 h incubation (Figure 2C, lower panel; Figure 2D, lower panel). At 4 h postincubation, nearly all of the HFn accumulated in lysosomes (Figure S5D). Thus, HFn appeared to be internalized and translocated into lysosomes. This is in contrast to the subcellular localization of HFn in BBB ECs (see Figure 2C).

Taken together, our results suggest that HFn possesses properties conducive with the aim of traversing the BBB for the purpose of targeting tumors in the brain.

HFn Distinguishes Glioma Tumors from Normal Brain Tissues. To confirm that HFn specifically targets tumor cells, we identified the exact location of IRdye800-HFn nanoparticles in mice (hereafter called Luc-mCherry-U87MG-tumor mice) bearing orthotopic luciferase-expressing mCherry$^+$ U87MG human glioma tumor. The position and size of the U87MG tumor in the brain of Luc-mCherry-U87MG-tumor mice were defined by measuring the bioluminescence (BLI) signal of the luciferase upon intraperitoneal injection of luciferin (Figure 3A and E); that is, two U87MG tumors were visualized, with the bigger one near the calvarium (Figure 3A). As shown in Figure 3B, i.v.-injected HFn nanocarriers accumulated in two areas that overlapped with those identified by bioluminescence. Near infrared fluorescence (NIRF) imaging following isolation of the main organs isolated from Luc-mCherry-U87MG-tumor mice confirmed HFn nanoparticle accumulation in the tumor-bearing brain (Figure 3C). In addition to the brain, liver and kidney, as the main organs for ferritin nanoparticle metabolism,[24,25] also exhibited strong HFn accumulation (Figure 3C and F).

To confirm that HFn distinguishes glioma tumors from normal brain tissues, we examined the margins of tumors indicated by signals of mCherry expressed in U87MG tumor cells and IRdye800-HFn, respectively, in whole brain tissue (Figure 3D, upper panel) and corresponding brain sections (Figure 3D, lower panel). As shown in Figure 3D, we found that both signals overlapped to a considerable degree, similar to the signals of mCherry and Cy5.5-labeled HFn (Figure 3G). Moreover, the amount of accumulated HFn nanocarriers was 10-fold higher in the tumor area compared to adjacent healthy brain tissue (Figure S3C).

DOI: 10.1021/acsnano.7b06969
ACS Nano XXXX, XXX, XXX−XXX

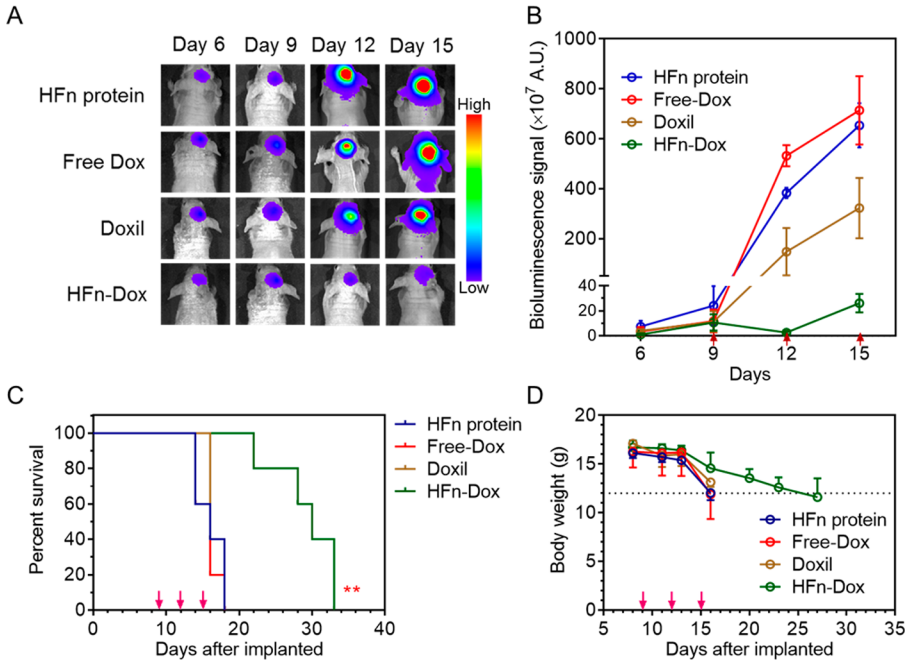

Figure 4. HFn-encapsulated Dox effectively improves antiglioma tumor activity. (A) *In vivo* BLI images of GBM tumor cells in orthotopic mice that were intravenously injected with different formulations, *i.e.*, HFn-Dox, Doxil, free Dox, and HFn protein. (B) Quantitative analysis (n = 5) of the BLI signals of (A). The red arrows indicate the time points of administering. (C) Animal survival curves in different groups. Asterisks indicate that the difference between HFn-Dox and free Dox or Doxil was statistically significant (Kaplan–Meier, p = 0.0019 and 0.0023, respectively). (D) Effect of different treatments on mouse body weight (mean ± SD, n = 5).

As shown in Figure S7, experiments with clinical glioma tissues support these findings. These results confirmed that, after crossing the BBB, HFn specifically targets and accumulates in tumor tissues.

Taken together, our results provide strong evidence that HFn is transported across the BBB *via* HFR, followed by specific targeting of glioma tumor cells in a highly cell-type-specific manner.

HFn Nanocarriers Kill Glioma Tumor. The ability to effectively overcome the BBB and the selective glioma targeting property of HFn nanocarrier may offer a therapeutic opportunity for treating brain cancers. To test this hypothesis, we used Dox-loaded HFn (HFn-Dox, prepared as we previously reported[24]) and measured its antiglioma activity in orthotopic luciferase-expressing U87MG tumor bearing mice.

The results of our characterization of HFn-Dox, including Cryo-EM, DLS, and SEC analysis, stability, and drug release of HFn-Dox are shown in Figure S10. The integrity of HFn-Dox nanoparticles after traversing the BBB was also confirmed. The orthotopic glioma mice exhibited severe body weight loss and short survival time (typical less than 18 days), as the growing tumor severely affected normal brain function.[31] The potential therapeutic window was chosen on the basis of the proliferation curve of U87MG tumor cells growing in the brain (Figure S8). HFn-Dox nanoparticles were i.v. injected at a Dox dose of 1 mg/kg mice weight three times every 3 days starting 9 days post-tumor cell implantation in the mouse brain. The same dose of free Dox and nontargeted liposomal Dox (Doxil) or HFn empty protein nanoparticles were also administrated as negative controls. On day 6 (before administration), 9, 12, and 15, the therapeutic responses indicated by the BLI signals were monitored and quantified.

The HFn-Dox treatment in the U87MG-bearing mice resulted in a visible regression of tumor growth (Figure 4A and B) and thus an extended survival time (median survival 30 days) (Figure 4C), which is a significant improvement over free Dox (Kaplan–Meier, p = 0.0019) as well as Doxil treatment (Kaplan–Meier, p = 0.0023). In contrast, tumors in HFn- or free-Dox-treated mice grew rapidly. Although Doxil exhibited slight inhibitory effects on tumor growth, the median survival time in Doxil-treated mice (16 days) differed little from that in free Dox or HFn protein treated groups (16 days and 16 days, respectively) due to its severe side effects[24] (Figure 4C,D). HFn-Dox treatment showed delayed body weight loss compared to the other three treatments (Figure 4D), which may be the combined result of effective tumor regression and lower toxicity. Together, these results indicate that HFn-Dox significantly suppresses the growth of orthotopic glioma tumors *in vivo*.

To investigate the potential side effects of HFn-Dox in mice, we evaluated their biosafety. Healthy BALB/c mice were i.v. injected with the same dose of HFn-Dox as the therapeutic dose used in brain tumor mice therapy. As shown in Figure S11, administration at these concentrations showed no significant effect on the body weight of healthy mice. None of the main organs exhibited any significant pathological changes.

DISCUSSION

In this study, we demonstrated that HFn nanocarriers specifically bind BBB ECs, traverse the BBB, and target glioma tumor cells *via* interaction with the HFR. Upon entering BBB ECs, our HFn nanocarrier accumulated in endosomes, but not in lysosomes, resulting in its effective crossing of the BBB. In contrast, upon entering glioma cells, nearly all of the HFn accumulated in the lysosomal compartment. In a proof-of-principle experiment using Dox-loaded HFn particles, tumor growth was clearly suppressed, and the life span of the tumor-

DOI: 10.1021/acsnano.7b06969
ACS Nano XXXX, XXX, XXX–XXX

bearing mice was substantially prolonged. This unexpected combination of properties renders HFn an ideal candidate for brain-tumor-specific therapy.

While both HFn nanocarriers and HFR (*e.g.*, TfR1) antibodies enter the BBB ECs, only HFn nanocarriers locate in endosomes and then traverse the BBB, whereas TfR1 antibodies accumulate in the lysosomes. The difference in localization between HFn and TfR1 antibodies is likely due to its different binding affinities with TfR1.[13,15] Chuang and colleagues have shown that high-affinity anti-TfR1 antibodies facilitate the trafficking of the antibody−TfR1 complex to lysosomes for degradation, while accumulation of low-affinity antibodies was found to be reduced in lysosomes of BBB ECs.[13] It has been previously reported that the binding affinity of the antibody used here is significantly higher than that of the HFn nanocarrier.[23] Thus, binding affinity with TfR1 may be the key factor that determines the subcellular location of HFn nanocarriers and anti-TfR1 antibodies in BBB ECs.

In contrast, when HFn nanocarriers enter the glioma tumor cells, nearly all accumulated in the lysosomes. As a matter of fact, several groups including ours demonstrated earlier that HFn nanocarriers accumulated in the lysosomes after they enter different types of tumor cells, such as human colon cancer cells,[25] breast cancer cells,[32] melanoma cells,[24] and pancreatic cancer cells.[33] The different behavior of HFn nanocarriers in BBB ECs and tumor cells may be due to the different expression levels of TfR1. Our results show that the expression of TfR1 in glioma cells is more than 10-fold higher than that of BBB ECs. Recently, Niewoehner *et al.* reported that the multivalent binding mode of TfR1 antibodies to TfR1 commonly results in their sorting into the lysosomal compartment, whereas antibodies with monovalent TfR1 binding mode accumulate less in lysosomes and more in endosomes.[14] Because of the symmetrical structure of HFn, we infer that there would be more than one binding site for TfR1 in the protein shell of HFn. Thus, when the amounts of TfR1 on tumor cells are excess, the interactions of HFn−TfR1 tend to exhibit a multivalent binding mode, which results in HFn accumulation in the lysosomes. Another possible explanation for the sorting behavior of HFn is that BBB ECs have better transcytosis ability than glioma tumor cells.[5] Thus, after entry into the cells, HFn nanocarriers tend to be transported across the BBB ECs, whereas in glioma tumor cells, HFn nanocarriers accumulate in the lysosomes.

In our *in vivo* animal experiments, we found that HFn was transported across the intact BBB via HFR; after crossing the BBB, HFn specifically recognized the HFR-positive glioma tumors and distinguished the tumor cells from normal brain tissues. Such glioma tumor targeting of HFn nanocarriers *in vivo* is likely related to the following phenomena: (1) Glioma tumor cells commonly express high levels of HFR (*e.g.*, TfR1), which are approximately 10−100-fold higher than those in normal cells;[34] (2) HFn nanocarriers are preferentially incorporated by receptor-positive cells, a process that occurs in a threshold-dependent manner, thus enabling HFn nanocarriers to specifically distinguish tumor cells from normal cells;[35] (3) a hallmark of glioma is the formation of new vasculature.[36] At the early stage of brain tumor vessel formation, the newly formed capillaries are still continuous but fenestrated, allowing the penetration of spherical molecules with less than 12 nm size.[37] The diameter of spherical HFn protein is 12 nm, an ideal size for EPR effects for macromolecular nanocarriers.[38] Thus, except for its active BBB-crossing and tumor-targeting abilities, HFn also possesses the passive targeting property for even small brain tumors. Our data clearly show that HFn nanocarriers are able to detect small U87MG orthotopic tumors (~1 mm) (Figure S3); thus HFn presents a promising tool for early diagnosis or treatment of brain tumor.

After encapsulating Dox (HFn-Dox), the HFn nanocarriers inhibited orthotopic tumor growth and substantially prolong the survival of tumor-bearing mice. Importantly, HFn nanocarriers exhibit a better tumor inhibition rate and lower side effects compared to nontargeted clinically approved Doxil, which further confirms the benefits of the active targeting property of the HFn nanocarrier. Moreover, previous studies established that the HFR (*e.g.*, TfR1) is widely expressed in various human brain tumors.[8,9] As a result, several therapies based on HFR targeting have already been evaluated in clinical trials.[39] Hence, the HFn nanocarrier is a promising candidate for clinical brain tumor therapy.

In addition, HFn-Dox exhibited excellent biosafety *in vivo*. In our previous report, we already demonstrated that HFn-Dox significantly reduced the cardiotoxicity of Dox, increasing the maximum tolerated dose of Dox from 5 mg/kg to 20 mg/kg. Importantly, 96 h after i.v. injection of HFn-Dox into healthy mice, over 70% of HFn-Dox was eliminated from the body *via* the kidney (into urine) and liver (into feces).[24] The accumulated dose of HFn-Dox in this study was 3 mg/kg. Thus, the administration of HFn-Dox did not induce significant toxicity in the liver, kidney, or spleen. Importantly, HFn-Dox did not exhibit significant toxicity to healthy brain tissues. The reasons for this lack of toxicity may be manifold. First, HFn nanocarriers specifically recognize glioma tumor cells. As a result, the accumulated HFn nanocarriers in the tumor area are more that 10-fold higher than that in the healthy brain tissues; second, HFn nanocarriers are preferentially incorporated by receptor-positive cells in a threshold-dependent manner. Here, we compared the uptake ratio of HFn in glioma tumor, BBB ECs, and astrocytes. The results demonstrated that glioma tumor cells take up more than 10-fold higher HFn than that of normal neuron cell astrocytes; no significant uptake of HFn was observed in normal neuron cells (Figure S9); lastly, the HFR (*e.g.*, TfR1)-mediated transcytosis is bidirectional.[40] In healthy brain tissues, the penetrating HFn nanocarriers accumulated near the blood vessels (Figures S2D and S3C). Since HFn nanocarriers did not accumulate in the normal brain cells, they may partially return to blood circulation.

CONCLUSION

Taken together, our HFn nanocarriers possess several important characteristics that are of advantage for translation into clinical brain tumor therapy.

First, HFn nanocarriers possess excellent biotoxicity/biodegradability. Naturally existing in humans, HFn nanocarriers consist of amino acids that do not activate inflammatory or immunological responses.[21]

Second, HFn nanocarriers possess high loading efficiency and controlled drug release properties. The nanocage architecture of HFn allows for easy encapsulating of a variety of drugs with high loading efficiency.[24] Moreover, the HFR (TfR1)-mediated endocytosis is a useful pathway for drug-selective delivery.[41] Our previous studies demonstrated that the HFR-mediated endocytosis endows HFn with a controlled drug release property.[24,25]

DOI: 10.1021/acsnano.7b06969
ACS Nano XXXX, XXX, XXX−XXX

Third, HFn nanocarriers possess excellent dual tumor-targeting properties. Without any ligand modification, HFn specifically recognizes tumor cells through HFR-mediated tumor targeting;[21] in addition, the outer diameter of HFn is 12 nm, which is ideal for anticancer nanomedicine because HFn can fully overcome the physiological barriers posed by the tumor microenvironment and passively penetrate the tumor tissues *via* EPR effects.[42] Both active and passive tumor targeting render HFn an excellent choice for tumor therapy *in vivo*.

Fourth, HFn nanocarriers are effectively produced in *E. coli* at a high yield (more than 300 mg/L in this work), and the loading process of drugs or imaging moieties inside the nanoparticle is relatively simple.

Lastly, HFn nanocarriers exhibit BBB-traversing and the glioma-targeting abilities, which render HFn nanocarriers to be promising candidates for effective brain tumor therapy.

On the basis of all of the above-mentioned properties of HFn, we propose that the HFn nanocarrier is an ideal nanocarrier for brain-tumor-specific therapy. Also, the HFn nanocarrier possesses the potential to serve as a therapeutic approach against a broad range of CNS diseases.

MATERIALS AND METHODS

Cellular Culture. The luciferase- and mCherry-transfected human glioblastoma cell line U87MG (U87MG-Luc-mCherry) was obtained from the Institute of Basic Medical Sciences, Chinese Academy of Medical Sciences, and the mouse brain endothelial cells bEnd.3 were obtained from ATCC. Both types of cells were cultured in DMEM medium (Sigma-Aldrich) containing 10% fetal calf serum (Sigma-Aldrich), penicillin (100 U/mL, Sigma-Aldrich), and streptomycin (100 μg/mL, Sigma-Aldrich) at 37 °C with 5% CO_2. U87MG cells were cultured in T-75 flasks (Corning) and passaged by trypsin-EDTA digestion twice a week.

The immortalized human brain capillary endothelial cell line hCMEC/D3 was obtained from INSERM, France. Cells were cultured in EBM-2 medium supplemented with growth factors, hydrocortisone, ascorbate, 2.5% fetal calf serum (Sigma-Aldrich), and antibiotics (Gibco Life Technologies Inc., UK) at 37 °C with 5% CO_2.

Cell-Binding Assays. The binding activities of HFn and LFn nanoparticles to mouse BBB EC bEnd.3 cells and human BBB EC hCMEC/D3 cells were detected using a FACSCalibur (Becton Dickinson) flow cytometry system and analyzed using Cell Quest software (Becton Dickinson). To perform the binding analysis, 100 μL detached brain endothelial cell suspensions (2.5×10^6 cells/mL) were incubated with 0.4 μM FITC-HFn for 45 min at 4 °C in phosphate-buffered saline (PBS) containing 0.3% bovine serum albumin (BSA). After three washes in cold PBS, cells were analyzed immediately using a FACSCalibur flow cytometry system. FITC-conjugated LFn protein was used as a negative control.

The expression of TIM-2 in mouse BBB EC bEnd.3 cells was detected by a FACSCalibur (Becton Dickinson) flow cytometry system. A 100 μL amount of detached bEnd.3 mouse brain endothelial cell suspensions (2.5×10^6 cells/mL) was incubated with rat anti-mouse TIM-2 monoclonal antibody (1:100, Clone RMT2-1, Santa Cruz) for 45 min at 4 °C in PBS containing 0.3% BSA. After three washes in cold PBS, cells were incubated with Alexa Fluor 488 goat anti-rat secondary antibody (1:200, A-11006, ThermoFisher). After another three washes in cold PBS, cells were analyzed immediately using a FACSCalibur flow cytometry system. Rat IgG protein was used as a negative control.

The expression of TfR1 in human BBB EC hCMEC/D3 was detected also by a FACSCalibur (Becton Dickinson) flow cytometry system. A 100 μL amount of detached hCMEC/D3 suspensions (2.5×10^6 cells/mL) was incubated with mouse anti-human TfR1 monoclonal antibody (1:100, CloneM-A712, BD Pharmingen) for 45 min at 4 °C in PBS containing 0.3% BSA. After three washes in cold PBS, cells were incubated with Alexa Fluor 488 goat anti-mouse secondary antibody (1:200, A-32723, ThermoFisher) and analyzed after another three washes in cold PBS using a FACSCalibur flow cytometry system. Mouse IgG protein was used as a negative control.

An antibody blocking assay was performed to test whether TIM-2 or TfR1 is the binding receptor of HFn to BBB EC cells. Briefly, 0.4 μM FITC-HFn was incubated with BBB EC cells in the presence or absence of a10-fold molar excess of anti-TIM-2 Ab (Clone RMT2-1, Santa Cruz) or mouse anti-human TfR1 monoclonal antibody (1:100, CloneM-A712, BD Pharmingen). After three washes in cold PBS, cells were analyzed immediately using a FACSCalibur flow cytometry system. FITC-conjugated LFn protein was used as a negative control.

Analysis of Cellular Uptake, Subcellular Localization, and Colocalization. The cellular uptake and subcellular localization of HFn or LFn nanoparticles and distributions of HFn protein in cells were studied by a confocal laser scanning microscope (CLSM) (Olympus FluoView FV-1000, Tokyo, Japan). Briefly, bEnd.3, hCMEC/D3, or U87MG cells were plated on poly-L-lysine-treated coverslips (BD Biosciences) and cultured in a six-well plate (Corning) for 12 h before using. After stimulation for 5 min, 1 h, 2 h, and 4 h with 1 μM FITC-HFn/FITC-LFn nanoparticles/rat anti-TIM-2 antibody (1:10, Clone RMT2-1, Santa Cruz)/mouse anti-human TfR1 monoclonal antibody (1:10, CloneM-A712, BD Pharmingen), cells were washed with PBS, fixed in 4% cold formaldehyde in PBS for 5 min, and then permeabilized with 0.1% Triton X-100. After three washes in PBS, cells were blocked in 5% normal goat serum for 30 min at room temperature. To observe the localization of antibodies, cells were incubated with Alexa Fluor 488 goat anti-rat secondary antibody for anti-TIM-2 antibody (1:200, A-11006, ThermoFisher) and Alexa Fluor 488 goat anti-mouse secondary antibody for anti-TfR1 antibody (1:200, A-32723, ThermoFisher) for 1 h at 37 °C. To visualize lysosomes, cells were incubated with a mouse anti-Lamp1 mAb (1:50, clone H4A3; Santa Cruz) at 37 °C for 1 h, then washed three times with PBS and incubated with goat anti-mouse IgG1 conjugated with AlexaFluor555 (1:500; Invitrogen) at 37 °C for 1 h. Finally, the nuclei of cells were stained by 4′,6-diamidino-2-phenylidole (DAPI, 1 μg/mL, Roche Applied Science) for 10 min at room temperature. The fluorescence signals were examined with a CLSM (Olympus FluoView FV-1000, Tokyo, Japan). A 60× oil objective was used to capture all images with a digital zoom factor of 2−4×. The colocalization analysis of HFn/Lamp1 and anti-TIM-2 antibody/Lamp1 was performed using the FluoView colocalization tool (Olympus FluoView FV-1000, Tokyo, Japan). Three experiments with at least 10 cells quantified per experiment were performed. The statistical analysis was done in Graphpad Prism (Graphpad Inc., version 6.02).

***In Vitro* Transcytosis Assay.** Mouse BBB EC bEnd.3 cells and human BBB EC hCMEC/D3 cells were used to generate an *in vitro* BBB model as previously reported.[14,43,44] BBB EC cells were plated on gelatin-coated 0.4 μm pore size Transwell plates (24 mm Transwell, Corning) at a density of 6×10^4 cells/cm^2 in culture media and were allowed to grow for 48−72 h to reach confluency. The transcytosis assay was performed when the trans-endothelial electrical resistance (TEER) of this model reached 100 Ω·cm^2. FITC-labeled HFn or LFn (100 μg) in fresh culture media was then added to the top (apical) chamber. Transcytosis of the ferritin proteins were determined by collecting samples from the bottom (basal) chamber at the time points of 30, 60, and 120 min, following the addition of the FITC-labeled ferritins. The concentration of ferritins in the basal chamber was analyzed based on the linear relation of protein concentration and FITC fluorescence determined in a spectrofluorometer Varioskan Flash spectral scanning multimode reader (ThermoFisher Scientific) using excitation at 490 nm and emission at 525 nm. Experimental conditions were prepared in triplicates.

Animal Models. All animal studies were performed following the ethics protocol approved by the Institutional Animal Care and Use Committee at the Institute of Biophysics, Chinese Academy of Sciences. Male BALB/c nude mice (6−7-week-old) were obtained from Vital River Laboratories (Beijing). Mice were housed under standard conditions with free access to sterile food and water. To establish the U87MG intracranial orthotopic glioblastoma mice model,

DOI: 10.1021/acsnano.7b06969
ACS Nano XXXX, XXX, XXX−XXX

mice were anesthetized using 2.0% isoflurane and then positioned in a stereotactic instrument. The top of the animal's head was cleaned with 70% ethanol and betadine. A linear skin incision was made over the bregma, and 3% hydrogen peroxide was applied to the periost with a cotton swab. A 27G needle was then used to drill a burrhole into the skull 0.5 mm anterior and 2 mm lateral to the bregma. A 10 μL gastight syringe (Hamilton) was then used to inject 10 μL of the U87MGcell suspension (1×10^6 cells in PBS) in the striatum at a depth of 2.5 mm from the dural surface. The injection was done slowly over 10 min. The burr hole was occluded with glue to prevent leakage of cerebrospinal fluid, and the skin was closed with surgical clips. For whole-body imaging, each tumor-bearing mouse was injected with dye-labeled ferritin nanoprobes (10 mg protein/kg body weight) *via* tail vain.

Bioluminescence Imaging and 3D Reconstruction. Bioluminescence imaging (BLI) was performed using the Xenogen IVIS Lumina II system (PerkinElmer, Waltham, MA, USA). Eight minutes after intraperitoneal injection of D-luciferin (150 mg/kg), animals were imaged, and the same procedure was repeated at the specified time. Imaging signals in regions of interest were quantified in units of mean photons per second per square centimeter per steradian ($p/s/cm^2/sr$). Three-dimensional bioluminescence tomography based on the Bayesian approach for reconstructing the U87MG orthotopic tumor mouse model was performed as previously reported,[45] and images were prepared by IVIS Living Image 3.0 software (PerkinElmer, USA).

Photoacoustic Imaging. All phantoms and *in vivo* photoacoustic imaging experiments were conducted using a multispectral photoacoustic tomography system (inVision, iTheraMedical GmbH, Munich, Germany). The system consists of a tunable laser with working wavelengths ranging from 680 to 960 nm. The light pulses excited photoacoustic signals were acquired using a multielements cylindrically focused ultrasound transducer. The phantom was made up of polyurethane with two cylindrical spaces inside for measuring the photoacoustic signals of the probes. Prior to the experimental procedure, animals were mounted on an animal holder with a thin plastic membrane to avoid directly touching the water in an imaging chamber, and they were moved horizontally under isoflurane anesthesia. Images were scanned slice by slice. Each slice (0.8 mm) was acquired 10 times at each moving step for averaging. Six different wavelengths, 715, 730, 760, 773, 800, and 850 nm, were used to generate multispectral photoacoustic information. The intracranial orthotopic glioblastoma mice models were scanned from head to neck at the time point of preinjection, 2 and 4 h postinjection of probes. The acquired data were reconstructed into images by a model-based method. We unmixed the signals of oxygen hemoglobin, dioxygen hemoglobin, and the probes by multispectral analyses to obtain more information.

A precision *xyz*-stage with a minimum step size of 1 μm was used to move the transducer and the fiber ring along a planar 2D trajectory. At every position, the acquired signal was averaged over two to four laser pulses. The time of arrival and the intensity of the laser pulses were recorded using a silicon photodiode (DET10A, Thorlabs). This information was used to synchronize the acquisition and compensate for pulse-to-pulse variations in laser intensity. The analog photoacoustic signals were amplified using a 30 dB preamplifier (5676/115VAC, Panametrics Olympus NDT) and digitized using an oscilloscope (Infinium 54825A, Agilent). The photoacoustic and ultrasound images were reconstructed as follows: the a-scan from each position of the transducer was band-pass filtered with 100% fractional bandwidth, which compensated for laser intensity variations and envelope detection. The a-scans were then combined to reconstruct a 3D intensity image of the target. No further postprocessing was done on the images. Ultrasound images were acquired using a 5 or 25 MHz transducer.

NIRF Imaging. All *ex vivo* and *in vivo* NIRF imaging experiments were conducted with an IVIS Spectrum imaging system (PerkinElmer, USA). For *in vivo* IRdye800-labeled probe imaging, the tumor mouse models were scanned at the time point of preinjection, 1, 3, 6, and 24 h postinjection of the probes into tail veins right after photoacoustic imaging. A filter set with excitation and emission wavelengths of 745 and 800 nm, respectively, was used to measure the fluorescent signal of IRdye800. For *in vivo* and *ex vivo* Cy5.5-labeled probe imaging, excitation and emission wavelengths of 673 and 707 nm, respectively, were used to measure the fluorescent signal of Cy5.5. To avoid the fluorescence quenching, the *ex vivo* imaging of the excised organs was performed immediately after mice were sacrificed without perfusion. Imaging data were processed and analyzed by IVIS Living Image 3.0 software (PerkinElmer, USA).

Therapy Studies. For therapy studies, 20 male BALB/c nude mice bearing U87MG tumors were randomly assigned into four groups (n = 5 mice per group). All mice were treated intravenously with drugs *via* vain tail on day 9, day 12, and day 15 postimplantation of U87MG cells. Drugs were administrated at 1 mg/kg Dox equivalent for free Dox, HFn-Dox, and Doxil, respectively, and at 24 mg/kg HFn equivalent for HFn-Dox and the HFn control. The BLI fluorescence imaging analysis was used to evaluate the therapeutic efficiency of different types of formulations from 5 to 30 days after tumor cells were implanted.

Fluorescence Imaging of Brain Tissues and Sections Using the in-House Stereotactic Microscopy System. The in-house stereofluorescence imaging of brain tissues and brain sections was performed as reported previously.[46] Briefly, a stereofluorescence microscope was coupled with a conventional camera and a low-temperature CCD (PIXIS CCD, Princeton Instruments, Trenton, NJ, USA) to acquire both white-light and fluorescent images. For measurement of IRdye800, a 785 nm diode laser was used (Ex = 775 nm, Em = 800 nm); for measurement of mCherry protein, a Leica M205FA automated fluorescence stereomicroscope was used (Ex = 585 nm, Em = 620 nm).

All of the fluorescent images of organs were acquired with an aperture of F1.4 and an exposure time of 0.1 s. The fluorescent images of brain slices were captured with an aperture of F1.4 and an exposure time of 1.0 s.

ASSOCIATED CONTENT

Supporting Information

The Supporting Information is available free of charge on the ACS Publications website at DOI: 10.1021/acsnano.7b06969.

Detailed descriptions of the preparation, labeling, and characterization of the HFn and LFn nanocarriers, formation and characterization of HFn-Dox, expression of HFR in BBB ECs, TEER measurements, coculture BBB model, analysis of HFn accumulation in the brain parenchyma, and histological staining assay (PDF)

AUTHOR INFORMATION

Corresponding Authors

*E-mail: fankelong@ibp.ac.cn.
*E-mail: jie.tian@ia.ac.cn.
*E-mail: yanxy@ibp.ac.cn.

ORCID

Kelong Fan: 0000-0001-6285-1933
João Conde: 0000-0001-8422-6792
Jie Tian: 0000-0002-9523-2271
Xiyun Yan: 0000-0002-7290-352X

Author Contributions

#K. Fan, X. Jia, and M. Zhou contributed equally to this work.

Author Contributions

K.L.F. and X.H.J. conceived the study and designed the experiments. X.H.J., K.L.F., M.Z., K.W., J.C., and J.H. performed the experiments. X.Y.Y. and J.T. reviewed, analyzed, and interpreted the data. K.L.F. and X.Y.Y. wrote the manuscript. All the authors contributed to the analysis of the data and discussed the manuscript.

DOI: 10.1021/acsnano.7b06969
ACS Nano XXXX, XXX, XXX−XXX

Notes

The authors declare no competing financial interest.

ACKNOWLEDGMENTS

We thank X.-W. Bian and L. Chen (Third Military Medical University of Chinese PLA) and G.-Z. Shi and D. Liu (Institute of Biophysics, CAS) for assistance with pathological analysis. We thank X.-J. Huang and G. Ji for excellent technical support in Cryo-EM imaging at the Transmission EM Facilities, Center for Biological Imaging, Institute of Biophysics. We thank J.-J. Zhang (Affiliated Hospital of Guangdong Medical University) for his professional suggestions on construction of the *in vitro* BBB model. We thank D. Peng (Xidian University) for his assistance of *in vivo* experiments and F. Wang (Institute of Biophysics, CAS) for his assistance in protein purification. We thank T. Juelich for linguistic assistance during the preparation of this manuscript. This work was financially supported by the National Natural Science Foundation of China (Nos. 31530026, 81527805, 61231004), Young Elite Scientist Sponsorship Program by CAST (2015QNRC001), China Postdoctoral Science Foundation (No. 2015M570158), the China Postdoctoral Science Special Foundation (No. 2016T90143), the Strategic Priority Research Program (Nos. XDA09030306, XDPB0304), the Key Research Program of Frontier Sciences (No. QYZDY-SSW-SMC013), and Chinese Academy of Sciences and National Key Research and Development Program of China (No. 2017YFA0205200).

REFERENCES

(1) Grabrucker, A. M.; Ruozi, B.; Belletti, D.; Pederzoli, F.; Forni, F.; Vandelli, M. A.; Tosi, G. Nanoparticle Transport Across the Blood Brain Barrier. *Tissue Barriers* **2016**, *4*, e1153568.

(2) Cloughesy, T. F.; Cavenee, W. K.; Mischel, P. S. Glioblastoma: From Molecular Pathology to Targeted Treatment. *Annu. Rev. Pathol.: Mech. Dis.* **2014**, *9*, 1−25.

(3) Parrish, K.; Sarkaria, J.; Elmquist, W. Improving Drug Delivery to Primary and Metastatic Brain Tumors: Strategies to Overcome the Blood-Brain Barrier. *Clin. Pharmacol. Ther.* **2015**, *97*, 336−346.

(4) Banks, W. A. From Blood-brain Barrier to Blood-Brain Interface: New Opportunities for CNS Drug Delivery. *Nat. Rev. Drug Discovery* **2016**, *15*, 275−292.

(5) Lajoie, J. M.; Shusta, E. V. Targeting Receptor-Mediated Transport for Delivery of Biologics Across the Blood-Brain Barrier. *Annu. Rev. Pharmacol. Toxicol.* **2015**, *55*, 613−631.

(6) Friden, P. M.; Walus, L. R.; Musso, G. F.; Taylor, M. A.; Malfroy, B.; Starzyk, R. M. Anti-Transferrin Receptor Antibody and Antibody-Drug Conjugates Cross the Blood-brain Barrier. *Proc. Natl. Acad. Sci. U. S. A.* **1991**, *88*, 4771−4775.

(7) Watts, R. J.; Dennis, M. S. Bispecific Antibodies for Delivery into the Brain. *Curr. Opin. Chem. Biol.* **2013**, *17*, 393−399.

(8) Prior, R.; Reifenberger, G.; Wechsler, W. Transferrin Receptor Expression in Tumors of the Human Nervous-System-Relation to Tumor Type, Grading and Tumor-Growth Fraction. *Virchows Arch. A: Pathol. Anat. Histopathol.* **1990**, *416*, 491−496.

(9) Recht, L.; Torres, C. O.; Smith, T. W.; Raso, V.; Griffin, T. W. Transferrin Receptor in Normal and Neoplastic Brain-Tissue-Implications for Brain-Tumor Immunotherapy. *J. Neurosurg.* **1990**, *72*, 941−945.

(10) Moos, T.; Morgan, E. H. Transferrin and Transferrin Receptor Function in Brain Barrier Systems. *Cell. Mol. Neurobiol.* **2000**, *20*, 77−95.

(11) Qian, Z. M.; Li, H.; Sun, H.; Ho, K. Targeted Drug Delivery *via* the Transferrin Receptor-Mediated Endocytosis Pathway. *Pharmacol. Rev.* **2002**, *54*, 561−587.

(12) Bell, R. D.; Ehlers, M. D. Breaching the Blood-Brain Barrier for Drug Delivery. *Neuron* **2014**, *81*, 1−3.

(13) Bien-Ly, N.; Yu, Y. J.; Bumbaca, D.; Elstrott, J.; Boswell, C. A.; Zhang, Y.; Luk, W.; Lu, Y.; Dennis, M. S.; Weimer, R. M.; Chung, I.; Watts, R. J. Transferrin Receptor (TfR) Trafficking Determines Brain Uptake of TfR Antibody Affinity Variants. *J. Exp. Med.* **2014**, *211*, 233−244.

(14) Niewoehner, J.; Bohrmann, B.; Collin, L.; Urich, E.; Sade, H.; Maier, P.; Rueger, P.; Stracke, J. O.; Lau, W.; Tissot, A. C.; Loetscher, H.; Ghosh, A.; Freskgard, P. O. Increased Brain Penetration and Potency of a Therapeutic Antibody Using a Monovalent Molecular Shuttle. *Neuron* **2014**, *81*, 49−60.

(15) Yu, Y. J.; Atwal, J. K.; Zhang, Y.; Tong, R. K.; Wildsmith, K. R.; Tan, C.; Bien-Ly, N.; Hersom, M.; Maloney, J. A.; Meilandt, W. J.; Bumbaca, D.; Gadkar, K.; Hoyte, K.; Luk, W.; Lu, Y.; Ernst, J. A.; Scearce-Levie, K.; Couch, J. A.; Dennis, M. S.; Watts, R. J. Therapeutic Bispecific Antibodies Cross the Blood-Brain Barrier in Nonhuman Primates. *Sci. Transl. Med.* **2014**, *6*, 261ra154.

(16) Gao, H.; Pang, Z.; Jiang, X. Targeted Delivery of Nano-Therapeutics for Major Disorders of the Central Nervous System. *Pharm. Res.* **2013**, *30*, 2485−2498.

(17) Chen, H.; Zhang, W.; Zhu, G.; Xie, J.; Chen, X. Rethinking Cancer Nanotheranostics. *Nat. Rev. Mater.* **2017**, *2*, 17024.

(18) Saraiva, C.; Praça, C.; Ferreira, R.; Santos, T.; Ferreira, L.; Bernardino, L. Nanoparticle-Mediated Brain Drug Delivery: Overcoming Blood−Brain Barrier to Treat Neurodegenerative Diseases. *J. Controlled Release* **2016**, *235*, 34−47.

(19) Pelaz, B.; Alexiou, C.; Alvarez-Puebla, R. A.; Alves, F.; Andrews, A. M.; Ashraf, S.; Balogh, L. P.; Ballerini, L.; Bestetti, A.; Brendel, C.; Bosi, S.; Carril, M.; Chan, W. C.; Chen, C.; Chen, X.; Chen, X.; Cheng, Z.; Cui, D.; Du, J.; Dullin, C.; et al. Diverse Applications of Nanomedicine. *ACS Nano* **2017**, *11*, 2313−2381.

(20) Cerna, T.; Stiborova, M.; Adam, V.; Kizek, R.; Eckschlager, T. Nanocarrier Drugs in the Treatment of Brain Tumors. *J. Cancer Metastasis Treat.* **2016**, *2*, 407−416.

(21) Fan, K.; Gao, L.; Yan, X. Human Ferritin for Tumor Detection and Therapy. *Wiley Interdiscip. Rev.: Nanomed. Nanobiotechnol.* **2013**, *5*, 287−298.

(22) Fan, K.; Cao, C.; Pan, Y.; Lu, D.; Yang, D.; Feng, J.; Song, L.; Liang, M.; Yan, X. Magnetoferritin Nanoparticles for Targeting and Visualizing Tumour Tissues. *Nat. Nanotechnol.* **2012**, *7*, 459−464.

(23) Li, L.; Fang, C. J.; Ryan, J. C.; Niemi, E. C.; Lebron, J. A.; Bjorkman, P. J.; Arase, H.; Torti, F. M.; Torti, S. V.; Nakamura, M. C.; Seaman, W. E. Binding and Uptake of H-ferritin are Mediated by Human Transferrin Receptor-1. *Proc. Natl. Acad. Sci. U. S. A.* **2010**, *107*, 3505−3510.

(24) Liang, M.; Fan, K.; Zhou, M.; Duan, D.; Zheng, J.; Yang, D.; Feng, J.; Yan, X. H-Ferritin-Nanocaged Doxorubicin Nanoparticles Specifically Target and Kill Tumors with a Single-Dose Injection. *Proc. Natl. Acad. Sci. U. S. A.* **2014**, *111*, 14900−14905.

(25) Zhao, Y.; Liang, M.; Li, X.; Fan, K.; Xiao, J.; Li, Y.; Shi, H.; Wang, F.; Choi, H. S.; Cheng, D.; Yan, X. Bioengineered Magneto-ferritin Nanoprobes for Single-Dose Nuclear-Magnetic Resonance Tumor Imaging. *ACS Nano* **2016**, *10*, 4184−4191.

(26) Fargion, S.; Arosio, P.; Fracanzani, A. L.; Cislaghi, V.; Levi, S.; Cozzi, A.; Piperno, A.; Fiorelli, G. Characteristics and Expression of Binding Sites Specific for Ferritin H-Chain on Human Cell Lines. *Blood* **1988**, *71*, 753−757.

(27) Fargion, S.; Fracanzani, A. L.; Brando, B.; Arosio, P.; Levi, S.; Fiorelli, G. Specific Binding Sites for H-Ferritin on Human Lymphocytes: Modulation During Cellular Proliferation and Potential Implication in Cell Growth Control. *Blood* **1991**, *78*, 1056−1061.

(28) Moss, D.; Powell, L. W.; Arosio, P.; Halliday, J. W. Characterization of the Ferritin Receptors of Human T Lymphoid (MOLT-4) Cells. *J. Lab. Clin. Med.* **1992**, *119*, 273−279.

(29) Chen, T. T.; Li, L.; Chung, D. H.; Allen, C. D.; Torti, S. V.; Torti, F. M.; Cyster, J. G.; Chen, C. Y.; Brodsky, F. M.; Niemi, E. C.; Nakamura, M. C.; Seaman, W. E.; Daws, M. R. TIM-2 is Expressed on B Cells and in Liver and Kidney and Is a Receptor for H-Ferritin Endocytosis. *J. Exp. Med.* **2005**, *202*, 955−965.

DOI: 10.1021/acsnano.7b06969
ACS Nano XXXX, XXX, XXX−XXX

(30) Han, J.; Seaman, W. E.; Di, X.; Wang, W.; Willingham, M.; Torti, F. M.; Torti, S. V. Iron Uptake Mediated by Binding of H-Ferritin to the TIM-2 Receptor in Mouse Cells. *PLoS One* **2011**, *6*, e23800.
(31) El Meskini, R.; Iacovelli, A. J.; Kulaga, A.; Gumprecht, M.; Martin, P. L.; Baran, M.; Householder, D. B.; Van Dyke, T.; Ohler, Z. W. A Preclinical Orthotopic Model for Glioblastoma Recapitulates Key Features of Human Tumors and Demonstrates Sensitivity to a Combination of MEK and PI3K Pathway Inhibitors. *Dis. Models Mech.* **2015**, *8*, 45−56.
(32) Li, X.; Zhang, Y.; Chen, H.; Sun, J.; Feng, F. Protein Nanocages for Delivery and Release of Luminescent Ruthenium(II) Polypyridyl Complexes. *ACS Appl. Mater. Interfaces* **2016**, *8*, 22756−22761.
(33) Lei, Y.; Hamada, Y.; Li, J.; Cong, L.; Wang, N.; Li, Y.; Zheng, W.; Jiang, X. Targeted Tumor Delivery and Controlled Release of Neuronal Drugs with Ferritin Nanoparticles to Regulate Pancreatic Cancer Progression. *J. Controlled Release* **2016**, *232*, 131−142.
(34) Daniels, T. R.; Bernabeu, E.; Rodriguez, J. A.; Patel, S.; Kozman, M.; Chiappetta, D. A.; Holler, E.; Ljubimova, J. Y.; Helguera, G.; Penichet, M. L. The Transferrin Receptor and the Targeted Delivery of Therapeutic Agents Against Cancer. *Biochim. Biophys. Acta, Gen. Subj.* **2012**, *1820*, 291−317.
(35) Sakamoto, S.; Kawabata, H.; Masuda, T.; Uchiyama, T.; Mizumoto, C.; Ohmori, K.; Koeffler, H. P.; Kadowaki, N.; Takaori-Kondo, A. H-Ferritin Is Preferentially Incorporated by Human Erythroid Cells through Transferrin Receptor 1 in a Threshold-Dependent Manner. *PLoS One* **2015**, *10*, e0139915.
(36) Hamza, M. A.; Mandel, J. J.; Conrad, C. A.; Gilbert, M. R.; Yung, W. K.; Puduvalli, V. K.; DeGroot, J. F. Survival Outcome of Early *versus* Delayed Bevacizumab Treatment in Patients with Recurrent Glioblastoma. *J. Neuro-Oncol.* **2014**, *119*, 135−140.
(37) Pinto, M. P.; Arce, M.; Yameen, B.; Vilos, C. Targeted Brain Delivery Nanoparticles for Malignant Gliomas. *Nanomedicine* **2016**, *12*, 59−72.
(38) Dreher, M. R.; Liu, W.; Michelich, C. R.; Dewhirst, M. W.; Yuan, F.; Chilkoti, A. Tumor Vascular Permeability, Accumulation, and Penetration of Macromolecular Drug Carriers. *J. Natl. Cancer Inst.* **2006**, *98*, 335−344.
(39) Voth, B.; Nagasawa, D. T.; Pelargos, P. E.; Chung, L. K.; Ung, N.; Gopen, Q.; Tenn, S.; Kamei, D. T.; Yang, I. Transferrin Receptors and Glioblastoma Multiforme: Current Findings and Potential for Treatment. *J. Clin. Neurosci.* **2015**, *22*, 1071−1076.
(40) Pardridge, W. M. Drug and Gene Targeting to the Brain with Molecular Trojan Horses. *Nat. Rev. Drug Discovery* **2002**, *1*, 131−139.
(41) Tortorella, S.; Karagiannis, T. C. Transferrin Receptor-Mediated Endocytosis: a Useful Target for Cancer Therapy. *J. Membr. Biol.* **2014**, *247*, 291−307.
(42) Chauhan, V. P.; Stylianopoulos, T.; Martin, J. D.; Popovic, Z.; Chen, O.; Kamoun, W. S.; Bawendi, M. G.; Fukumura, D.; Jain, R. K. Normalization of Tumour Blood Vessels Improves the Delivery of Nanomedicines in a Size-Dependent Manner. *Nat. Nanotechnol.* **2012**, *7*, 383−388.
(43) Alvarez, J. I.; Dodelet-Devillers, A.; Kebir, H.; Ifergan, I.; Fabre, P. J.; Terouz, S.; Sabbagh, M.; Wosik, K.; Bourbonniere, L.; Bernard, M.; van Horssen, J.; de Vries, H. E.; Charron, F.; Prat, A. The Hedgehog Pathway Promotes Blood-Brain Barrier Integrity and CNS Immune Quiescence. *Science* **2011**, *334*, 1727−1731.
(44) Podjaski, C.; Alvarez, J. I.; Bourbonniere, L.; Larouche, S.; Terouz, S.; Bin, J. M.; Lecuyer, M. A.; Saint-Laurent, O.; Larochelle, C.; Darlington, P. J.; Arbour, N.; Antel, J. P.; Kennedy, T. E.; Prat, A. Netrin 1 Regulates Blood-Brain Barrier Function and Neuro-inflammation. *Brain* **2015**, *138*, 1598−1612.
(45) Feng, J.; Jia, K.; Qin, C.; Yan, G.; Zhu, S.; Zhang, X.; Liu, J.; Tian, J. Three-Dimensional Bioluminescence Tomography Based on Bayesian Approach. *Opt. Express* **2009**, *17*, 16834−16848.
(46) Fang, C.; Wang, K.; Zeng, C.; Chi, C.; Shang, W.; Ye, J.; Mao, Y.; Fan, Y.; Yang, J.; Xiang, N.; Zeng, N.; Zhu, W.; Fang, C.; Tian, J. Illuminating Necrosis: From Mechanistic Exploration to Preclinical Application Using Fluorescence Molecular Imaging with Indocyanine Green. *Sci. Rep.* **2016**, *6*, 21013.

DOI: 10.1021/acsnano.7b06969
ACS Nano XXXX, XXX, XXX−XXX